POAC'17
Busan, KOREA

Proceedings of the 24th International Conference on
Port and Ocean Engineering under Arctic Conditions
June 11-16, 2017, Busan, Korea

Brittle Failure Simulation of Ice Beam Using a Fully Lagrangian Particle Method

D. Ren[1], J.-C. Park[1*], S.-C. Hwang[2], S.-Y. Jeong[3], H.-S. Kim[4]
[1] Dept. of Naval Architecture & Ocean Engineering, Pusan National University (PNU), Busan, Korea
[2] Offshore Plant Research Division, Korea Research Institute of Ships and Ocean Engineering (KRISO), Daejeon, Korea
[3] Ship Hydrodynamics Research Group (Ice Model Basin), Korea Research Institute of Ships and Ocean Engineering (KRISO), Daejeon, Korea
[4] Dept. of Naval Architecture & Ocean Engineering, Inha Technical College, Incheon, Korea

ABSTRACT

A realistic numerical simulation technology using a particle-based fluid-structure interaction (FSI) model is combined with a brittle fracture algorithm to predict the fluid-ice-structure interaction. With respect to the failure of ice, it is modeled as a brittle fracture of elastic body by applying a novel FSI model based on the Moving Particle Semi-implicit (MPS) method. For verifying the developed fracture algorithm, a series of numerical simulation for 3-point bending tests with ice beam are performed and compared with the experiments carried out in the ice room. And then, for the application of the developed FSI model, a dropping water droplet interacting with a cantilever ice beam is simulated with and without the fracture algorithm. As the results from the simulation, it is seen that the consequent effects of fracture that might be occurred in the process of FSI simulation is available to be studied.

KEY WORDS: Brittle fracture, 3-point bending problem, Ice fracture, Fluid-ice-structure interaction, MPS (Moving Particle Semi-implicit) method

INTRODUCTION

In Arctic environment, ice accumulation plays a critical role as extremely high loads acting on the moored structures or the structures operating in ice-covered waters. The floating ice loads on the Arctic structures affect serious structural damages and safety for not only stationary operating offshore platforms but also sailing vessels in icy environments. Especially, when the icebreaker conducting icebreaking operations, the interaction of the crushed ice and marine propulsor has become an important factor affecting the performance and safety of the ship. Primary consideration for the Arctic transportations will be safety, effectiveness and cost. In order to evaluate a new design of ice strengthen vessel, physical model testing or numerical simulation should be required. To perform such simulations, the simulation technology of fluid-ice-structure interaction has become a necessary prerequisite.

Most of the fluid-structure interaction (FSI) simulation was performed by grid system (Hübner, et. al., 2004). When fracture is engaged, however, the grid system is interfering and the meshes need to be separated or decomposed to represent numerically the crack propagation. To solve these problems, therefore, a relatively complex algorithm should be required. In this respect, the meshless method is less restrictive from such matters.

Up to now, there are many researchers studied on the fracture by mesh or meshless method. Chan (Chan, 1981) studied the fracture toughness and creep behavior of ice by Finite Element Method (FEM). Sakharov (Sakharov et. al., 2015) carried out experiment of fixed end beam bending test with lake ice and compared the experimental results with the finite element simulation. Abbas (Abbas et. al., 2010) proposed two model-independent approaches based on Extended Finite Element Method (XFEM), which the author claim to be independent of the fracture model consideration. Sepehri (Sepehri, 2014) studied the hydraulic fracture propagation pattern used XFEM. Peixiang (Peixiang et al., 2013) studied he dynamic fracture problem in functional graded material based on Element-Free Galerkin Method (EFGM). Bui (Bui, 2008) presented a study of large deformation and failure flows of geo-material use Smoothed Particle Hydrodynamics (SPH). Tan (Tan et al., 2009) simulate the microscopic machining process of ceramics by considering the fracture and damage. Beckmann (Beckmann et. al., 2014) studied concrete fracture phenomena. Both of them used DEM model to achieve that. In recent, especially, there are also some research activities for numerical simulations to handle the ice breakup feature during the ice-structure interaction and treat broken ice as discrete-continuum material using the discrete element method (DEM). (Shen et al., 1987; Lepparanta et al., 1990; Hopkins, 1998; Hansen and Løset, 1999a, b; Selvadurai and Sepehr, 1999; Hopkins and Shen, 2001; Dai et al, 2004; Polojarvi and Tuhkuri, 2009; Zhan et al., 2010; Karulin and Karulina, 2011; Lau et al., 2011; Sun and Shen, 2012; Xu et al., 2012; Ji et al., 2013; Metrikin and Løset, 2013; Morgan, et al., 2015). However, most of DEM-based simulations concerned with ice floes have performed under no consideration of fully interacting with sea water.

In the present study, a realistic numerical simulation technology for predicting the fluid-ice-structure interaction has been newly developed using a particle-based FSI model which is combined with a brittle fracture algorithm. With respect to failure of ice, it is modeled as a brittle fracture of elastic by applying a novel FSI model based on the Moving Particle Semi-implicit (MPS) method (Hwang et al., 2014; 2016). To validate the developed fracture algorithm, the 3-point bending simulation with ice beam is performed and compared with the experiments which was carried out in a cold room. And then, for the application of FSI model, the dropping water droplet interacting with a cantilever ice beam is simulated comparatively with and without the fracture algorithm.

GOVERNING EQUATIONS

The momentum conservation equation for both of fluid and structure can be expressed as:

$$\frac{D\vec{u}}{Dt} = -\frac{1}{\rho}\nabla\cdot\sigma + \vec{f} + \vec{g} \tag{1}$$

where, ρ, t, $\vec{u}$, σ, $\vec{f}$, $\vec{g}$ indicate the density of fluid, time, velocity vector, stress tensor, external force and the gravity acceleration, respectively. The stress tensor σ is defined for fluid and structure analysis differently. For fluid, the stress tensor consists of a gradient of pressure and a viscosity term. For structure, the stress tensor is composed of normal stress and shear stress.

$$\sigma_{ij}^{F} = -P\delta_{ij} + \frac{\mu^{F}}{2}\left(\frac{\partial u_i}{\partial x_j} + \frac{\partial u_j}{\partial x_i}\right) \tag{2}$$

$$\sigma_{ij}^{S} = \lambda^{S}\frac{\partial \Delta x_k}{\partial x_k}\delta_{ij} + \frac{\mu^{S}}{2}\left(\frac{\partial \Delta x_i}{\partial x_j} + \frac{\partial \Delta x_j}{\partial x_i}\right) \tag{3}$$

where, P, μ^{F}, λ^{S} μ^{S} u Δx indicate the pressure and viscosity coefficient of fluid, the first and second Lamé's parameters, and the components of velocity and displacement.

Governing Equations of Fluid

By introducing Eq. (2) into Eq. (1), we obtain the momentum conservation equations of fluid, also known as Navier-Stokes equation. And in order to solve the pressure term by the relationship between the density and the divergence of the velocity, we also introduced the mass conservation equation as governing equation:

$$\frac{D\bar{u}}{Dt} = -\frac{1}{\rho_F}\nabla P + \nu\nabla^2\bar{u} + \vec{f}_{S_{to}F} + \bar{g} \tag{4}$$

$$\frac{D\rho_F}{Dt} + \rho_F\left(\nabla\cdot\bar{u}\right) = 0 \tag{5}$$

where, ρ_F, t, $\bar{u}$, $\vec{f}_{S_{to}F}$, $\bar{g}$, ν indicate the density of fluid, time, velocity vector, coupling force acting on the fluid boundary, gravity acceleration and the kinematic viscosity, respectively.

Governing Equations of Structure

By introducing Eq. (3) into Eq. (1), we obtain the momentum conservation equations of structure as:

$$\frac{D\bar{u}}{Dt} = \frac{1}{\rho_s}\nabla\cdot\left(\lambda_s tr\left(\varepsilon\right) + 2\mu_s\varepsilon\right) + \vec{f}_{F_{to}S} + \bar{g} \tag{6}$$

where, ρ_s, $\vec{f}_{F_{to}S}$, $\bar{g}$, ε imply the density of structure, stress tensor, load acting on the structure and the gravity acceleration, respectively.

And the Lame's constants λ_s and μ_s can be calculated by Young's modulus E and Poisson ratio ν_s as:

$$\lambda_s = \frac{E\nu_s}{\left(1+\nu_s\right)\left(1-2\nu_s\right)} \quad \mu_s = \frac{E}{2\left(1+\nu_s\right)} \tag{7}$$

To consider the rotation of structure particles, the angular momentum conservation equation was introduced as:

$$I\frac{D\vec{\omega}}{Dt} = \vec{r} \times \vec{f}_{shear} \tag{8}$$

where, I, $\vec{\omega}$, $\vec{r}$, $\vec{f}_{shear}$ indicate the moment of inertia, angular velocity, position vector and shear force, respectively.

Fluid-Structure Interaction Algorithm

A concept diagram of the FSI coupling system which is based on the improved MPS-based model (Hwang et al., 2014; 2016) is illustrated in Figure 1. After the fluid analysis is completed in a time step, the coupling force to structure analysis is calculated by integrating the pressure of fluid on the surface of structure. And then, the structure analysis is performed considering the coupling force from the fluid. Consequentially, the updated position of structure particles acts a role of new boundary condition and acceleration at the new interface is given as the coupling force to fluid analysis in next time step.

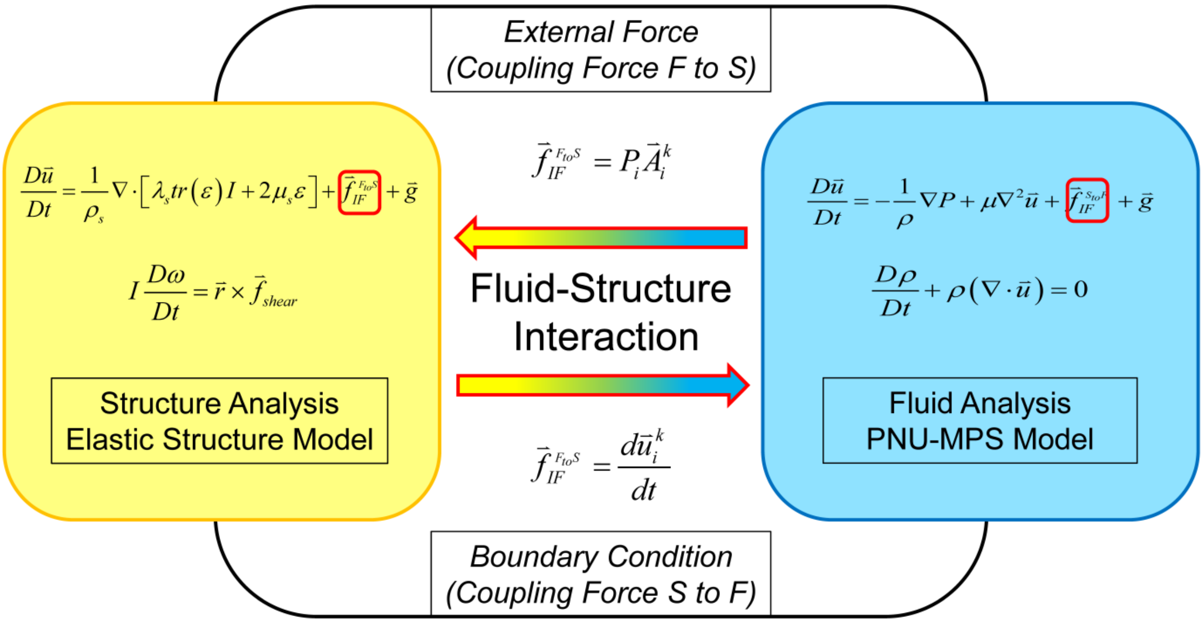

Figure 1. Concept diagram of FSI coupling procedure

In the calculation procedure, the prediction–correction solution algorithm is introduced for fluid analysis based on the PNU-MPS method (Lee et al., 2011). Firstly, the intermediate velocity is obtained from the viscous, coupling force and gravity terms explicitly as below:

$$\vec{u}_i^* = \vec{u}_{i,F}^k + \Delta t\left(\nu^F\nabla^2\vec{u}_i^k + \vec{f}_{i,S_{to}F}^k + \vec{g}\right) \tag{9}$$

where Δt is the time step and the superscript k implies time step number. Also, the coupling force $\vec{f}_{i,S_{to}F}$ can be defined by the acceleration of the interface of structure domain as:

$$\vec{f}_{i,S_{to}F} = \frac{d\vec{u}^{k}_{IF,F}}{dt} \tag{10}$$

After calculating the intermediate velocity by Eq. (9), the pressure field of fluid at time step $k+1$ is obtained implicitly by solving the Pressure Poisson Equation (PPE) as follows:

$$\nabla^2 P^{k+1}_{i,F} = \frac{\rho_F}{\Delta t}\left(\nabla\cdot\vec{u}^{*}\right)_i + \gamma\frac{\rho_F}{\Delta t^2}\frac{n^0 - n^k_i}{n^0} \tag{11}$$

where γ is a blending parameter considered as 0.03 (Lee et al., 2011), n^0 is the particle number density of initial arrangement and n^k is the particle number density at the k-th time step obtained as:

$$n_i = \sum_{j\neq i} w_F\left(\left|\vec{r}_j - \vec{r}_i\right|\right) \tag{12}$$

$$w_F = \begin{cases} \dfrac{r_e}{r} - 1 & 0 \le r \le r_e \\ 0 & r > r_e \end{cases} \tag{13}$$

In the correction step, finally, the new velocity at the time step $k+1$ is updated by taking the summation of intermediate velocity and pressure gradient term in Eq. (14).

$$\vec{u}^{k+1}_{i,F} = \vec{u}^{*}_i - \frac{\Delta t}{\rho_F}\nabla P^{k+1}_i \tag{14}$$

$$\vec{r}^{k+1}_{i,F} = \vec{r}^{k}_{i,F} + \Delta t\vec{u}^{k+1}_{i,F} \tag{15}$$

In Eq. (14), the Gradient Correction (GC) scheme (Khayyer and Gotoh, 2011) is used for calculating the pressure gradient term.

After completing the fluid analysis, the structure analysis is performed according to Hwang et. al.(2014; 2016). as:

$$\frac{D\vec{u}^{k+1}_{i,S}}{Dt} = \frac{1}{\rho_S}\nabla\cdot\left(\lambda_S\varepsilon^{k}_{ll}\right) + \frac{1}{\rho_S}\left[2\mu_S\nabla^2\left(\Delta\vec{x}\right)^{k}_{i,S}\right] + \vec{f}^{k}_{F_{to}S} + \vec{g} \tag{16}$$

where $\left(\Delta\vec{x}\right)^{k}_{i,S}$ is the displacement of the particle i from its initial location and ε_{ll} the strain rate represented as follows:

$$\varepsilon_{ll} = \varepsilon_{ii} + \varepsilon_{jj} + \varepsilon_{kk} = \frac{d}{n^0_i}\sum_{j\neq i}\frac{\left|\vec{x}^{k}_{j,S} - \vec{x}^{k}_{i,S}\right| - \left|\vec{x}^{0}_{j,S} - \vec{x}^{0}_{i,S}\right|}{\left|\vec{x}^{0}_{j,S} - \vec{x}^{0}_{i,S}\right|} w\left(\left|\vec{x}^{0}_{j,S} - \vec{x}^{0}_{i,S}\right|\right) \tag{17}$$

And a coupling force $\vec{f}^{k}_{F_{to}S}$ in Eq. (16) can be calculated by integrating the pressure on the interface as:

$$\vec{f}^{\,k}_{F_{to}S} = \int_{IF} P^{k+1}_{i,F} d\vec{s} = \frac{\sum_j P_{j_F} w\left(\left|\vec{x}_{j,F} - \vec{x}_{i,IF}\right|\right)}{\sum_j w\left(\left|\vec{x}_{j,F} - \vec{x}_{i,IF}\right|\right)} \tag{18}$$

where $\vec{x}_{i,IF}$ represents the position vector of the fluid-solid interface corresponding to the structure particle i and is calculated by the following formula (Antoci et. al., 2007).

$$\vec{r}_{i_{surf}} = \vec{r}_i + 0.5 l_0 \hat{n}_i \tag{19}$$

where l_0 is the initial particle length and $\hat{n}_i$ the normal vector of structure particle i.

For more detail description on the FSI algorithm, refer to Hwang et al. (2016; 2016).

Figure 2 shows the computational procedure of numerical algorithm for FSI simulation

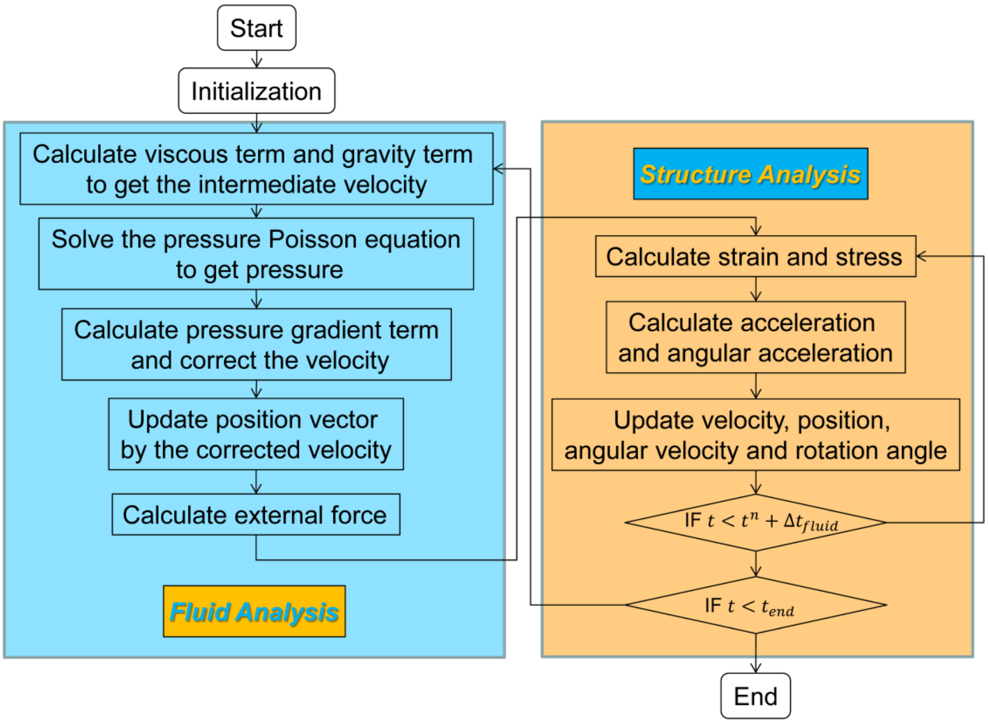

Figure 2. Computational procedure of numerical algorithm for FSI simulation

Brittle Failure

In the present study, the maximum normal stress criterion is used for a failure criteria of brittle fracture (Juvinall & Marshek, 2006), i.e. a brittle material will fail when the maximum normal stress, σ_1, exceeds the uniaxial tensile strength of the material, σ_f, as:

$$\sigma_1 \geq \sigma_f \tag{27}$$

Since the maximum normal stress that causes the failure may occur in any direction, we consider the rotation of stress tensor to obtain the maximum normal stress as follows:

$$\begin{aligned}\tilde{\sigma} = R^T \sigma R &= \begin{bmatrix} \cos\alpha & \sin\alpha \\ -\sin\alpha & \cos\alpha \end{bmatrix} \begin{bmatrix} \sigma_{xx} & \sigma_{yx} \\ \sigma_{xy} & \sigma_{yy} \end{bmatrix} \begin{bmatrix} \cos\alpha & -\sin\alpha \\ \sin\alpha & \cos\alpha \end{bmatrix} \\ &= \begin{bmatrix} \cos^2\alpha\sigma_{xx} + 2\cos\alpha\sin\alpha\sigma_{xy} + \sin^2\alpha\sigma_{yy} & \left(\cos^2\alpha - \sin^2\alpha\right)\sigma_{xy} + \cos\alpha\sin\alpha\left(\sigma_{yy} - \sigma_{xx}\right) \\ \left(\cos^2\alpha - \sin^2\alpha\right)\sigma_{xy} + \cos\alpha\sin\alpha\left(\sigma_{yy} - \sigma_{xx}\right) & \sin^2\alpha\sigma_{xx} - 2\cos\alpha\sin\alpha\sigma_{xy} + \cos^2\alpha\sigma_{yy} \end{bmatrix}\end{aligned} \tag{28}$$

From the above equation, the first normal components of stress, $\tilde{\sigma}_{n1}$, can be written as:

$$\tilde{\sigma}_{n1} = \tilde{\sigma}\left(\cos\alpha\right) = \cos^2\alpha\sigma_{xx} + 2\cos\alpha\sqrt{1-\cos^2\alpha}\sigma_{xy} + \left(1-\cos^2\alpha\right)\sigma_{yy} \tag{29}$$

In Eq. (29), the stress tensor is a function of rotation angle and the maximum stress in the normal direction should be satisfied to the following equation as:

$$\frac{\partial\sigma_{n1}}{\partial\cos\alpha} = 2\cos\alpha\left(\sigma_{xx} - \sigma_{yy}\right) + 2\frac{1-2\cos^2\alpha}{\sqrt{1-\cos^2\alpha}}\sigma_{xy} = 0 \tag{30}$$

The above equation can be rewritten as:

$$\cos\alpha\left(\sigma_{xx} - \sigma_{yy}\right) + \frac{1-2\cos^2\alpha}{\sqrt{1-\cos^2\alpha}}\sigma_{xy} = 0 \tag{31}$$

In general, Eq. (31) becomes a quadratic equation as:

$$\chi^2 - \chi + \frac{B}{\left(A+4B\right)} = 0 \tag{32}$$

where $\chi = \cos^2\alpha$, $A = \left(\sigma_{xx} - \sigma_{yy}\right)^2$, $B = \sigma_{xy}^2$.

Finally, the following equation can be obtained as the solution of Eq. (32):

$$\chi = \cos^2\alpha = \frac{1}{2} \pm \frac{1}{2}\sqrt{1 - \frac{4B}{A+4B}} \tag{33}$$

If the direction angle α for the maximum normal stress is obtained from Eq. (33), therefore, the corresponding maximum normal stress $\tilde{\sigma}_{\max}(=\sigma_1)$ can be determined by substituting α into Eq. (29).

In addition, there is another way to consider the maximum normal stress, so-called as the first principal stress. Because the maximum normal stress is indicated over the crack propagation direction, all components of shear stress should be zero, which means the first principal stress becomes the largest eigenvalue of the stress matrix. Hence, the direction of the maximum normal stress is the eigenvector corresponding to the eigenvalue of the stress matrix.

In the numerical process, when a particle i is judged that the crack occurs locally, a spring-like relationship will be disconnected with the neighboring particle j which is located opposite to the crack plane within the effective radius r_e. For any pair of two particles i and j in the vicinity of the crack, as long as they meet the following two conditions, the mutual influence each other will be eliminated by setting the value of weight function zero:

i) A pair particle needs to locate on both sides of the crack plane and can expressed as:

$$\left[\left(\vec{r}_i-\vec{r}_c\right)\cdot\hat{n}_c\right]\left[\left(\vec{r}_j-\vec{r}_c\right)\cdot\hat{n}_c\right]<0 \tag{34}$$

where, $\vec{r}_c=\left(\vec{r}_i+\vec{r}_j\right)/2$ implies the midpoint between two particles i and j, and $\hat{n}_c$ the direction of crack propagation as given in $\hat{n}_c=\left(\cos\alpha,\ \sin\alpha\right)$.

ii) One of two particles needs to be located opposite to the crack as:

$$\begin{gathered}\left|\left\{\left(\vec{r}_i-\vec{r}_c\right)-\left[\left(\vec{r}_i-\vec{r}_c\right)\cdot\hat{n}_c\right]\hat{n}_c\right\}\right|\le C_w l_0\\ \text{or}\\ \left|\left\{\left(\vec{r}_j-\vec{r}_c\right)-\left[\left(\vec{r}_j-\vec{r}_c\right)\cdot\hat{n}_c\right]\hat{n}_c\right\}\right|\le C_w l_0\end{gathered} \tag{35}$$

where, $C_w l_0$ should be determined in a range of $\frac{l_0}{2}\le C_w l_0\le r_e$ and C_w can be set at $\sqrt{d}/2$ to avoid discontinuous crack capturing especially in diagonal direction.

SIMULATION RESULTS

Simulation of Three-Point Bending Test

To validate the developed fracture algorithm, a series of numerical simulation of 3-point bending test with ice beam made of fresh water is performed and compared with the experimental data obtained from the experiment which was independently conducted in a cold room at Korea Maritime and Ocean University.

Figure 4 shows the schematic view of the three-point bending test. The distance between two simple support points is 180mm and the thickness of ice specimen is 40mm. A concentrated load with a constant speed of 0.0025m/s is applied to the midpoint of the ice beam.

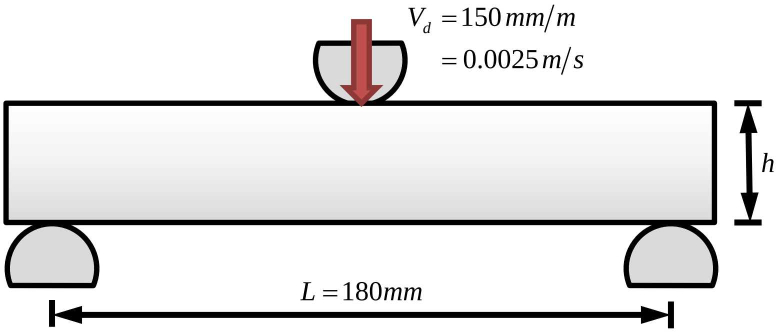

Figure 4. Schematic view of three-point bending test with ice beam

Photo 1 shows the typical snapshots of three-point bending test before and after crack of ice beam. It is seen clearly that a vertical crack appears just below the point where the load is acting when the load is large enough, which directly leads to the breakage of the ice beam.

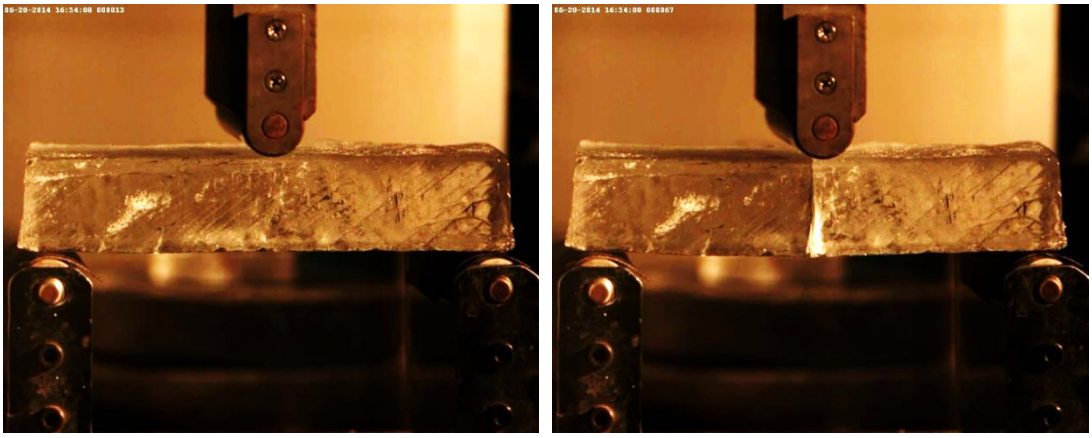

Photo 1. Experimental photos of three-point bending test with ice beam before (left) and after (right) cracking

From the experiment, the failure load $P_{\max}$ and deformation on the loading point $\Delta\delta$ were measured and the material properties of ice beam, such as Young's modulus E, flexural strength σ_f and flexural strain ε_f, were calculated as:

$$E = \frac{1}{4w}\left(\frac{L}{h}\right)^3 \frac{P_{\max}}{\Delta\delta} \tag{36}$$

$$\sigma_f = \frac{3}{2}\frac{P_{\max} L}{wh^2} \tag{37}$$

$$\varepsilon_f = \frac{6h\Delta\delta}{h^2} \tag{38}$$

where, w and h are the width and thickness of specimen.

The summarized experimental results are listed in Table 1.

Table 1. Summary of experiments for three-point bending test with ice beam

	Raw data				Calculation results		
Exp. No.	$w(m)$	$h(m)$	$P_{\max}(N)$	$\Delta\delta(m)$	$E(MPa)$	$\sigma_f(MPa)$	ε_f
02	0.082	0.038	500.1	6e-4	270.084	1.140	0.0042
03	0.084	0.044	411.9	4e-4	209.822	0.684	0.0032
04	0.081	0.040	588.4	9e-4	183.875	1.226	0.0067
05	0.079	0.039	441.3	1e-3	137.300	0.992	0.0072
10	0.082	0.037	323.6	1.15e-3	98.775	0.778	0.0079

In the simulation, the Young's modulus and flexural strength are used as the input data for material properties of ice beam. The Poisson's ratio is assumed to be 0.3. The time step and particle length are set at 10^{-6} s and 2×10^{-3} m, respectively.

The time-sequential snapshots of crack path and distribution of horizontal normal stress are shown in Figure 5. Before cracks appeared at t=0.0334s, the tensile stress is observed at lower part and compressive stress separated near central position where the concentrated load acts at upper part. As the crack evolves at t=0.0335s and 0.0339s, the concentration of horizontal stress is evident. Eventually the ice beam is completely broken at t=0.0342s and the corresponding stress is relived.

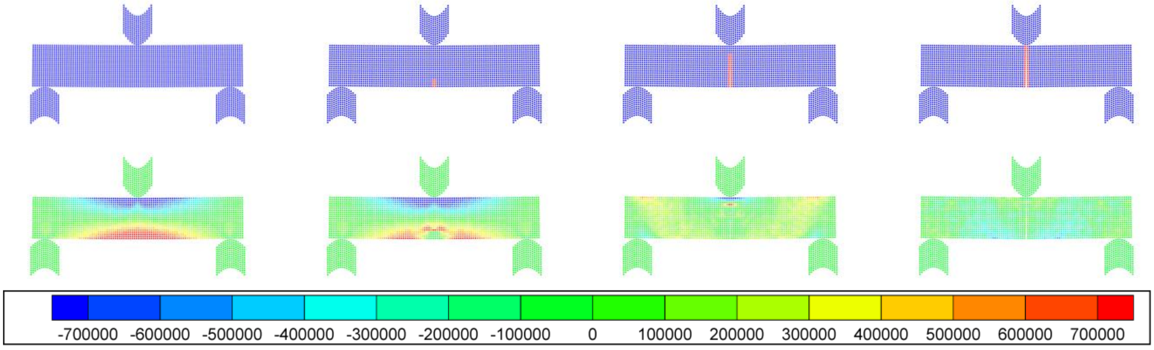

(a) t=0.0334s (b) t=0.0335s (c) t=0.0339s (d) t=0.0342s

Figure 5. Snapshots of crack path (upper) and normal stress in *x*-direction (lower)

Figure 6 shows the time history of horizontal normal stress at two middle points on top and bottom surface of the ice beam. The stress curves increase gradually with small elastic vibration before fracture as time increasing due to the assumption that the structure is considered as elastic material. And then after the fracture, the stresses dramatically decrease near zero.

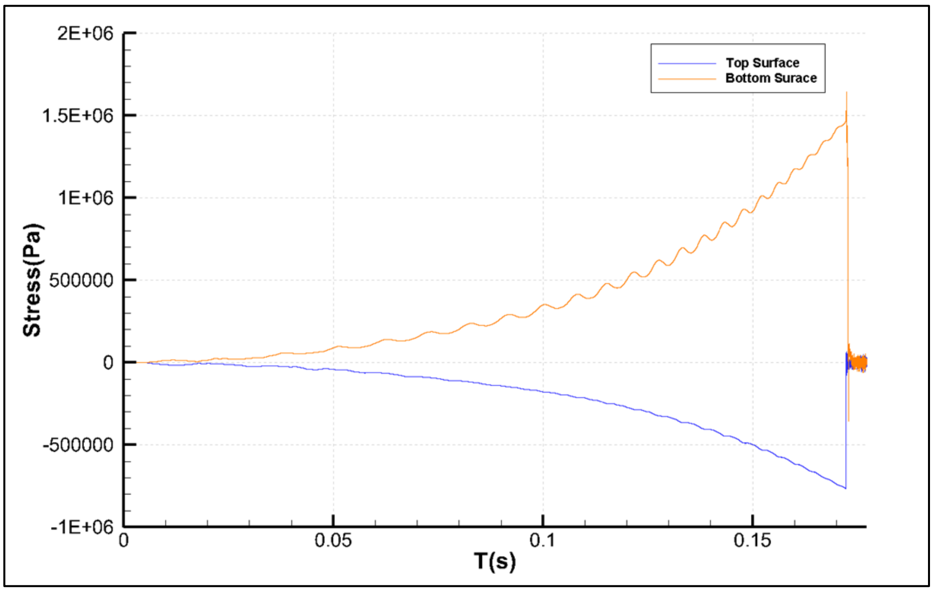

Figure 6. Time history of stress at two mid-points on top and bottom surface of beam

Finally, the flexural strains of the present simulation are compared with those of experiment in Figure 7. Overall agreements are quite good, but it tends that the deviation with the experiment becomes larger if the Young's modulus of the materials becomes smaller. The maximum error between both is below 7.5 percent.

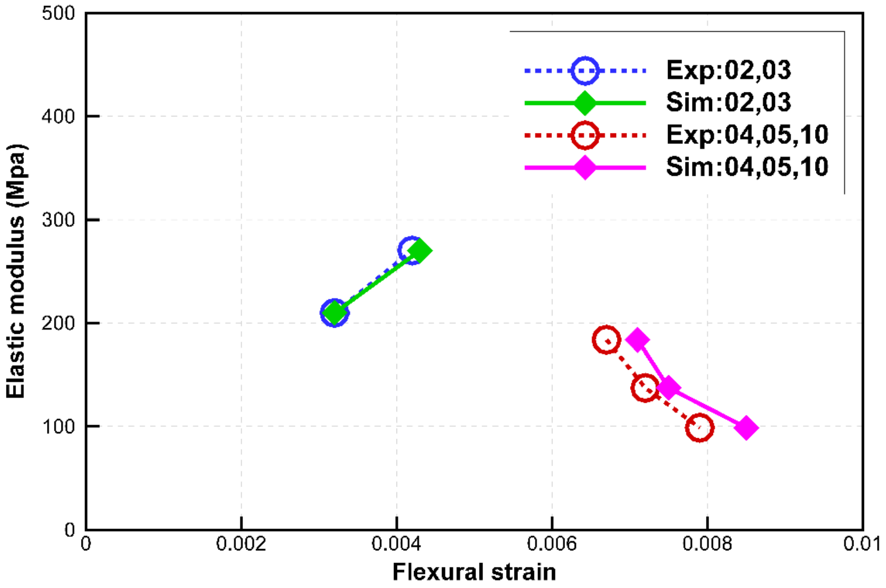

Figure 7. Comparison of flexural strain with experiments

FSI Simulation with Fracture Model

A dropping water droplet interacting with a cantilever ice beam is carried out for the application of FSI model. Figure 10 shows an initial setup for FSI simulation. The length and thickness of the ice beam are 0.5m and 0.05 m, respectively. The left end is fixed and the square water droplet with 0.1 m is falling down with the initial velocity of 9 m/s above the free end of the beam. The material properties of the cantilever ice beam are set the same as case 02 of 3-point bending test with the Young's modulus of 270.084 MPa, the Poisson's ratio of 0.3 and the flexural strength of 1.140 MPa. The time step for fluid and structure analysis are 1×10^{-5} s and 1×10^{-7} s, respectively, and the particle size is 2.5×10^{-3} m.

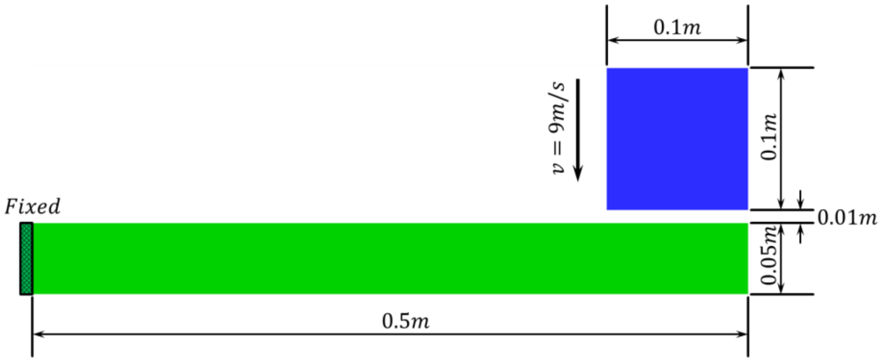

Figure 10. Schematic view and dimension of FSI simulation

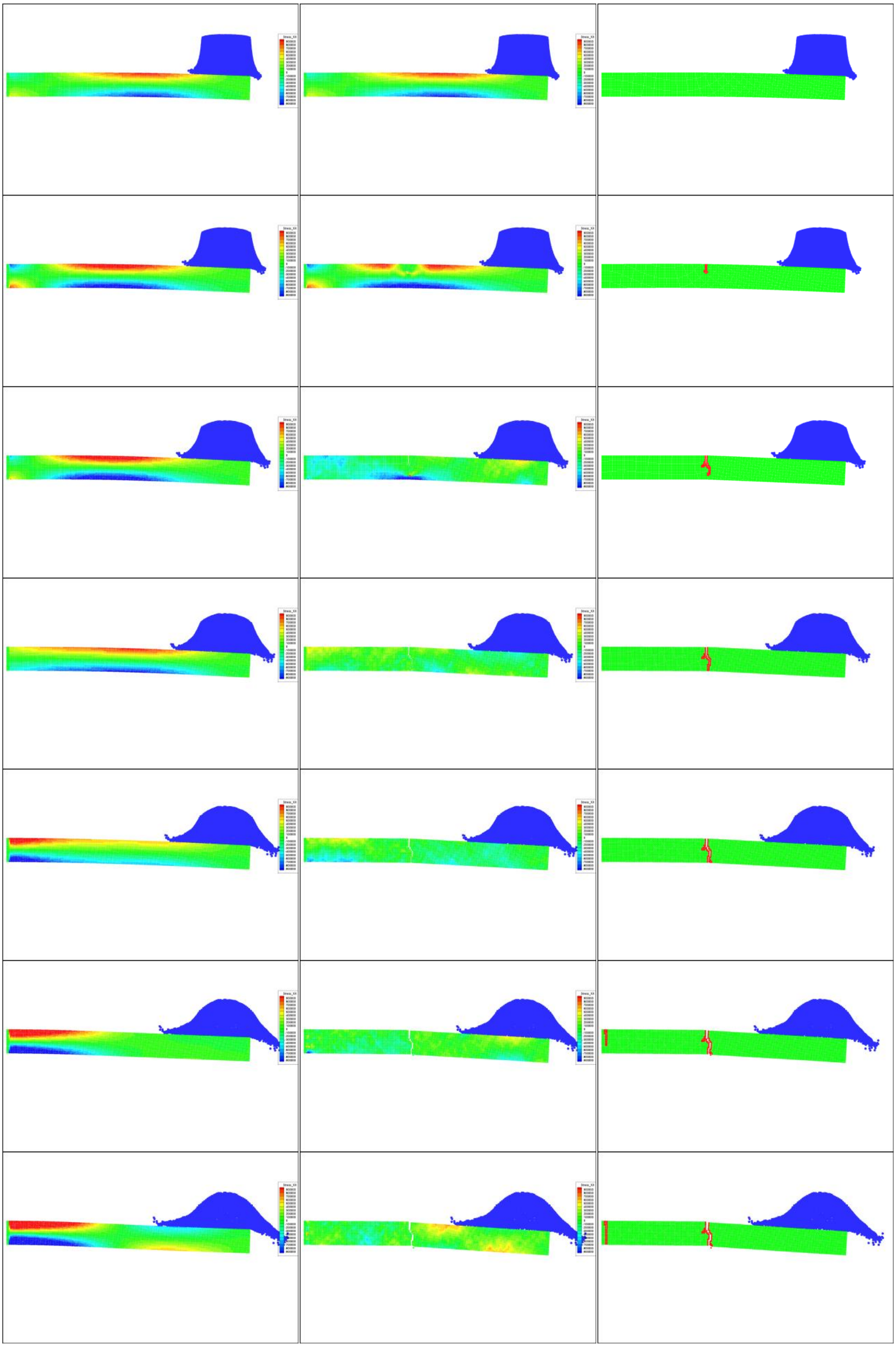

Figure 11. Snapshots of FSI simulation without failure (left), with failure (middle) and the crack path (right) from t=0.004s to t=0.01s with the step of 0.001s

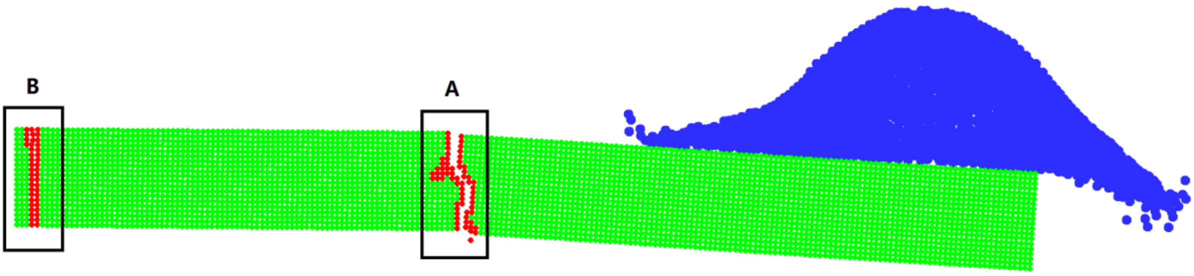

Figure 12. Definition of corresponding positions A and B

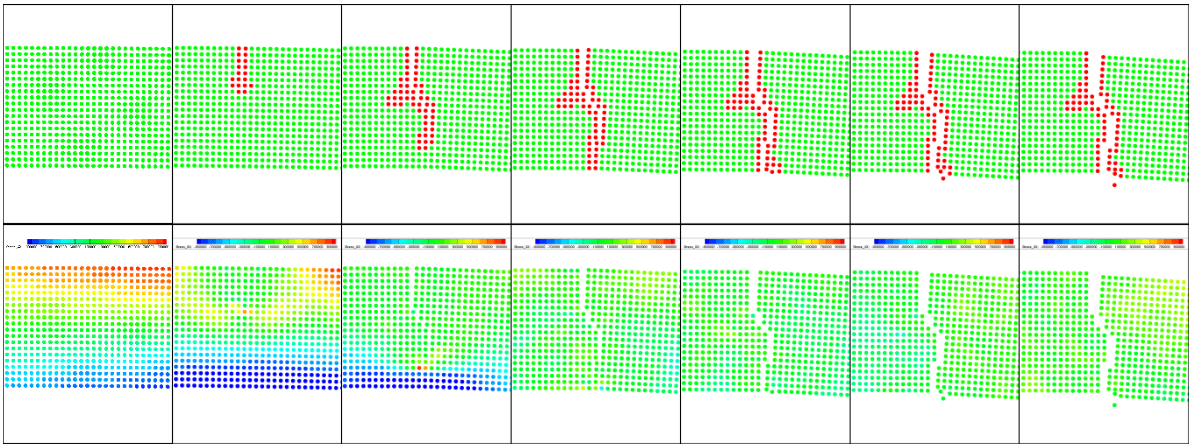

Figure 13. Snapshots of the failure path (upper) and horizontal normal stress distribution (below) at position A from t=0.004s to t=0.01s with interval of 0.001s

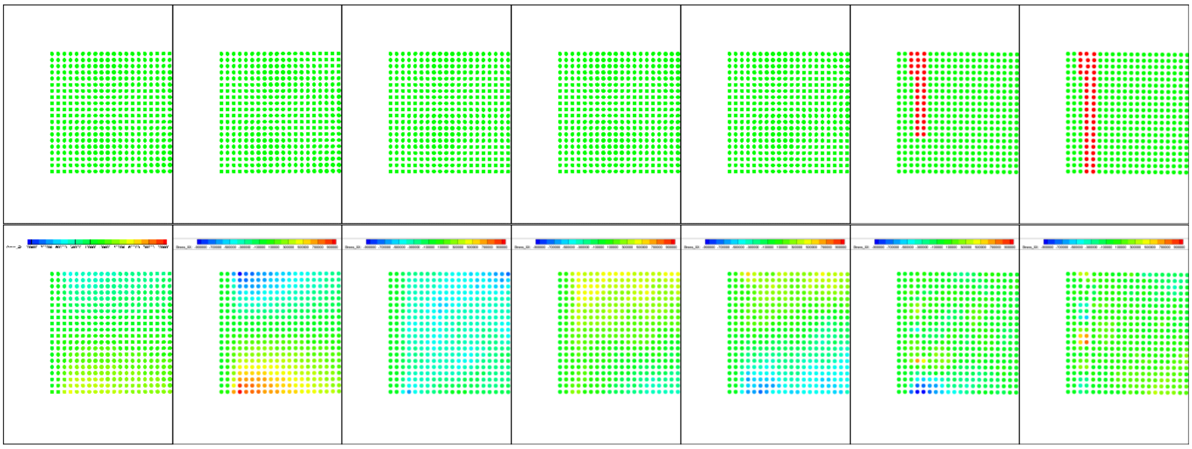

Figure 14. Snapshots of the failure path (upper) and the horizontal normal stress distribution (below) at position B from t=0.004s to t=0.01s with interval of 0.001s

Figure 11 illustrates the time-sequential snapshots for FSI simulation from t=0.004s to 0.01s with interval of 0.001s. The first and second column are the cases without and with the brittle failure algorithm, respectively, and the last column the crack path of ice in the FSI simulation with the failure algorithm. It can be shown that the failure occurs from where the local stress exceeds the critical value, and the dynamic behavior and stress distribution over the beam are completely different from the simulation without the failure algorithm.

A series of snapshots for local stress distribution and crack propagation around two different positions A and B marked in Figure 12 are depicted in Figures 13 and 14. It is observed the crack occurs where the stress is concentrated and location of stress concentration moves according to the front of crack propagation. At the same time, the corresponding stress distribution becomes unstable, which is whereby resulted in the direction of crack propagation unpredictably changed. Thus, small differences in conditions would reproduce completely different simulation results. It makes to predict accurately these kinds of problems difficult.

CONCLUSIONS

A realistic numerical simulation technology using a particle-based Fluid-Structure Interaction (FSI) model combined with a brittle fracture algorithm has been developed to simulate the fluid-ice-structure interaction problems. The failure of ice is modeled as a brittle fracture of elastic by applying a novel FSI model based on the Moving Particle Semi-implicit (MPS) method. The developed numerical algorithm of fracture was validated through the comparison with the experiments in a cold room for 3-point bending tests with ice beam. It was seen that the brittle failure was successfully simulated and the acceptable range of error was obtained within 7.5% compare to the experiments. After then, for the application of FSI model associated with the fracture algorithm, the numerical simulation of the dropping water droplet interacting with a cantilever ice beam was carried out comparatively with and without the fracture algorithm. From the simulation, it can be said that the consequent effects of fracture that might be occurred in the process of FSI simulation are available to be studied.

ACKNOWLEDGEMENTS

This work was supported by the IT R&D program of MOTIE/KEIT. [10060329, Development of numerical simulator for environmental load on ship and offshore in polar region]

REFERENCES

Antoci, C., Gallati, M., & Sibilla, S., 2007. Numerical simulation of fluid–structure interaction by SPH. *Computers & Structures,* 85(11), pp. 879-890.

Abbas, S., Alizada, A., & Fries, T. P., 2010. Model-independent approaches for the XFEM in fracture mechanics. *Int J Numer Methods Eng,* 1, pp. 0-10.

Beckmann, B., Schicktanz, K., & Curbach, M. 2014. *DEM Simulation of Concrete Fracture Phenomena.*

Bui, H. H., Fukagawa, R., Sako, K., & Ohno, S. (2008). Lagrangian meshfree particles method (SPH) for large deformation and failure flows of geomaterial using elastic–plastic soil constitutive model. *International Journal for Numerical and Analytical Methods in Geomechanics,* 32(12), pp. 1537-1570.

Chan, H. K. D., 1981. *Creep and fracture simulation of ice using the finite element method.* Ph.D. McMaster University.

Dai, M., Shen, H.H., Hopkins, M.A., Ackley, S.F., 2004. Wave rafting and the equilibrium pancake ice cover thickness. *Journal of Geophysical Research*, 109, C07023.

Hansen, E.H., Løset, S., 1999. Modelling floating offshore units moored in broken ice: model description. *Cold Regions Science and Technology,* 29, 97–106.

Hopkins, M.A., 1998. Four stages of pressure ridging. *Journal of Geophysical Research*, 103, 21883–21891.

Hopkins, M.A., Shen, H.H., 2001. Simulation of pancake-ice dynamics in wave field. *Annals of Glaciology*, 33, 355–360.

Hwang, S.C., Khayyer, A., Gotoh, H., & Park, J.C., 2014. Development of a fully lagrangian MPS-based coupled method for simulation of fluid–structure interaction problems. *Journal of Fluids and Structures,* 50, pp. 497-511.

Hwang, S.C., Park, J.C., Gotoh, H., Khayyer, A., & Kang, K.J., 2016. Numerical Simulation of Sloshing Flows with Elastic Baffles by Using a Particle-based Fluid–Structure Interaction Analysis Method. *Ocean Engineering,* 118, pp. 227-241.

Hübner, B., Walhorn, E., & Dinkler, D., 2004. A monolithic approach to fluid–structure interaction using space–time finite elements. *Computer methods in applied mechanics and engineering,* 193(23), pp. 2087-2104.

Ji, S., Li, Z., Li, C., Shang, J., 2013. Discrete Element Modeling of Ice Loads on Ship Hulls in Broken Ice Fields. *Acta Oceanologica Sinica,* 32(11), 50-58.

Juvinall, R. C., & Marshek, K. M., 2006. *Fundamentals of machine component design (Vol. 83).* John Wiley & Sons: New York.

Karulin, E.B., Karulina, M.M., 2011. Numerical and physical simulations ofmoored tanker behaviour. *Ship and Offshore Structures*, 6(3), 179–184.

Khayyer, A., & Gotoh, H., 2010. A higher order Laplacian model for enhancement and stabilization of pressure calculation by the MPS method. *Applied Ocean Research,* 32(1), pp. 124-131.

Khayyer, A., & Gotoh, H., 2011. Enhancement of stability and accuracy of the moving particle semi-implicit method. *Journal of Computational Physics,* 230(8), pp. 3093-3118.

Koshizuka, S., & Oka, Y., 1996. Moving-particle semi-implicit method for fragmentation of incompressible fluid. *Nuclear science and engineering,* 123(3), pp. 421-434.

Lau, M., Lawrence, K.P., Rothenburg, L., 2011. Discrete Element Analysis of Ice Loads on Ships and Structures. *Ships and Offshore Structures,* 6(3), 211-221.

Lee, B.H., Park, J.C., Kim, M.H., & Hwang, S.C., 2011. Step-by-step improvement of MPS method in simulating violent free-surface motions and impact-loads. *Computer methods in applied mechanics and engineering,* 200(9), pp. 1113-1125.

Lepparanta, M., Lensu, M., Lu, Q.M., 1990. Shear flow of sea ice in the Marginal Ice Zone with collision rheology. *Geophysica*, 25(1–2), 57–74.

Metrikin, I., Løset, S., 2013. Nonsmooth 3D Discrete Element Simulation of a Drillship in Discontinuous Ice. *Proceedings of the 22nd International Conference on Port and Ocean Engineering under Arctic Conditions*, Espoo, Finland.

Morgan, D., Sarracino, R., KcKenna, R., Thijssen, J.W., 2015. Simulation of Ice Rubbling against Conical Structures Using 3D DEM. *Proceedings of the 23rd International Conference on Port and Ocean Engineering under Arctic Conditions*, Trondheim, Norway.

Polojarvi, A., Tuhkuri, J., 2009. 3D discrete numerical modelling of ridge keek punch through tests. *Cold Regions Science and Technology*, 56, 18–29.

Peixiang, H., Ziran, L., & Changchun, W., 2013. An element-free Galerkin method for dynamic fracture in functional graded material. *In ICF10*, Honolulu (USA) 2001.

Sakharov, A., Karulin, E., Marchenko, A., Karulina, M., Sodhi, D., & Chistyakov, P., 2015. Failure Envelope of the Brittle Strength of Ice in the Fixed-End Beam Test (Two Scenarios). *In 23rd International Conference on Port and Ocean Engineering Under Arctic Conditions,* Trondheim, Norway.

Selvadurai, A.P.S., Sepehr, K., 1999. Two-dimensional discrete element simulations of ice-structure interaction. *International Journal of Solids and Structures*, 36, 4919–4940.

Sepehri, J., 2014. *Application of extended finite element method (XFEM) to simulate hydraulic fracture propagation from oriented perforations.* Ph.D. Texas Tech University.

Shen, H.H., Hibler, W.D., Lepparanta, M., 1987. The role of floe collisions in sea ice rheology. *Journal of Geophysical Research*, 92(C10), 7085–7096.

Sun, S., Shen, H.H., 2012. Simulation of pancake ice load on a circular cylinder in a wave and current field. *Cold Regions Science and Technology*, 78, 31–39.

Tan, Y., Yang, D., & Sheng, Y., 2009. Discrete element method (DEM) modeling of fracture and damage in the machining process of polycrystalline SiC. *Journal of the European ceramic society*, 29(6), pp. 1029-1037.

Tanaka, M., & Masunaga, T., 2010. Stabilization and smoothing of pressure in MPS method by Quasi-Compressibility. *Journal of Computational Physics*, 229(11), pp. 4279-4290.

Xu, Z., Tartakovsky, A.M., Pan, W., 2012. Discrete-element model for the interaction between ocean waves and sea ice. *Physical Review E*, 85, 016703.

Zhan, D., Agar, D., He, M., Spencer, D., Molyneux, D., 2010. Numerical simulation of ship maneuvering in pack ice. *Proceedings of the ASME 2010 29th International Conference on Ocean, Offshore and Arctic Engineering*, Shanghai, China, OMAE2010-21109.